Journal of Physics: Photonics



PAPER

OPEN ACCESS

RECEIVED
3 August 2025

REVISED
5 September 2025

ACCEPTED FOR PUBLICATION
24 September 2025

PUBLISHED
7 October 2025



# Design and function of a vertical micro-cavity optical parametric oscillator

**Ryotatsu Yanagimoto**[1], **Ouri Karni**[1], **Edwin Ng**, **Marc Jankowski**, **Timothy P McKenna** and **Thibault Chervy**[*]

NTT Research, Inc. Physics & Informatics Laboratories, 940 Stewart Dr, Sunnyvale, CA 94085, United States of America

[1] These authors contributed equally to this work.

[*] Author to whom any correspondence should be addressed.

**E-mail:** thibault.chervy@ntt-research.com

**Keywords:** nano-photonics, non-linear optics, quantum optics

## Abstract

Optical parametric oscillators (OPOs) have emerged as highly versatile platforms for signal processing, machine learning, and all-optical computation. In particular, integrated photonic circuits have demonstrated an efficient and scalable route to build OPO networks through time-multiplexing. However, for tasks requiring massive parallelism with low latency, spatial multiplexing with vertical micro-cavities is a more natural approach to overcome the shoreline density limits of edge-emitting photonics. To this end, we propose an approach to realizing vertical micro-cavity OPOs (VCOPOs) leveraging recent developments in micro-optical fabrication techniques. We consider thin film $LiNbO_3$-filled dielectric micro-cavities as a case study, but the approach taken here is readily extended to any $\chi^{(2)}$ nonlinear medium. Based on conservative industrial fabrication tolerances, we predict a minimal foot-print of ca. $5 \times 5\,\mu m^2$, while achieving oscillation thresholds in the microwatts range. Advanced fabrication methods open a path toward sub-$\mu$W oscillation threshold, with a ratio of single-photon non-linear coupling rate to dissipation rate $g/\kappa > 5\%$. We propose a theoretical framework for the classical and quantum operation of two dimensional arrays of VCOPOs, and discuss potential applications such as surface emitting devices, spatially multi-mode parametric amplifiers and squeezers, as well as optical simulators of classical and quantum Hamiltonians.

## 1. Introduction

An optical parametric oscillator (OPO) is a paradigmatic nonlinear photonic device, in which parametric down-conversion of pump photons produces signal and idler photons. Despite such a simple working mechanism, the range of functions that an OPO can fulfill is surprisingly broad. OPOs have long been used as coherent light sources, whose wavelength could be widely tuned by varying phase-matching conditions [1–3]. Leveraging the nonlinear behavior of the OPO, an optical power limiting function can be realized [4]. Beyond such classical functionalities, OPOs found multiple quantum use cases such as sources for entangled photon pairs [5], squeezed lasers [6], sensors for quantum statistics of weak signals [7, 8], and contributed to enhancing the sensitivity of gravitational-wave detectors [9]. Furthermore, *multiple* OPOs, when coupled together as a network, can realize emergent functions that a single OPO cannot achieve. Using each OPO as an emulator of an Ising spin, coherent Ising machines (CIMs) composed of an OPO network can solve combinatorial optimization problems [10, 11]. It has been shown that a network of OPOs can even constitute a Turing-complete computational system [12].

The functions of OPOs in these different roles is fundamentally connected to the specific geometry they are realized in. For instance, a free-space OPO with large, bulky, nonlinear elements enables handling high laser powers and tunable phase-matching conditions. In contrast, the confinement of light into narrow waveguides on photonic chips offer high local intensities, resulting in extremely low OPO thresholds, which are essential for delicate signal processing and for quantum photonics [13–15]. OPOs realized in long

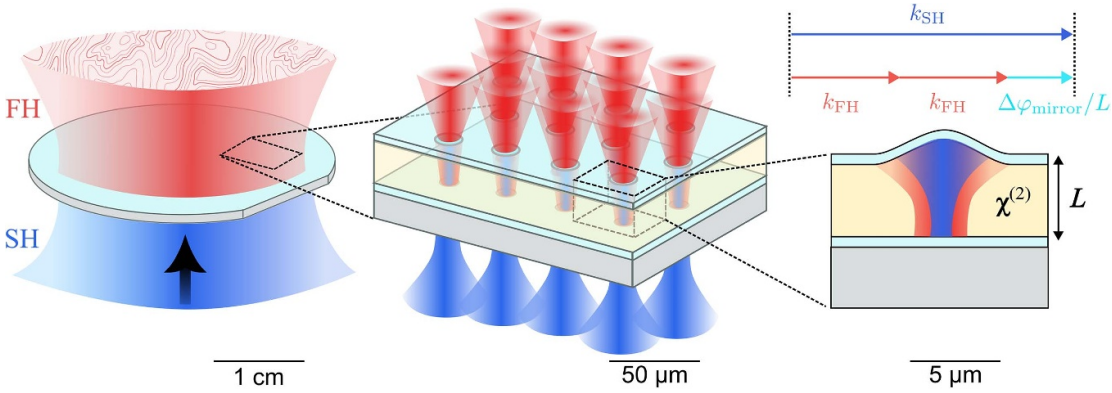


**Figure 1.** Pictorial representation of a wafer-scale VCOPO meta-surface (left), an array of VCOPO pixels (center), and a cross-section of a single VCOPO device (right). The scale bars represent the approximate length scales of the devices. The top right diagram shows the cavity phase-matching scheme, where the phase-mismatch between fundamental harmonics and second harmonics $2k_{FH} - k_{SH}$ over half a cavity round-trip is compensated by the extra phase accumulation by the mirror reflection $\Delta\varphi_{mirror}$.

fiber-based loops or in race-track geometries can support thousands of modes, which are the key to the speed and the computation power of CIMs [10, 11], and other neuromorphic computing devices [16]. Even an OPO without mirrors has been demonstrated, realizing simple and reliable device operation [17]. Thus, the future exploration of novel functions of OPOs will be unavoidably tied to the conception of new, unique, geometries.

In this work, we propose a new design strategy for vertical micro-cavity OPOs (VCOPOs) based on integrated micro-optics, quantitatively analyze their performance, and discuss potential applications. As shown in figure 1, the proposed VCOPO is composed of a thin film of $\chi^{(2)}$ nonlinear material, sandwiched between highly reflective dielectric mirrors. The pump and signal beams are coupled in and out using free-space focusing optics, and the phase-matching conditions are ensured by phase engineering of the dielectric mirrors, lifting the need for conventional techniques like birefringent phase-matching [18] or periodic poling [19]. As such, VCOPOs have several unique advantages compared to conventional geometries. First, the small footprint of each 'cell' and two-dimensional integrability could enable high scalability, while also maintaining high nonlinear efficiency. Second, the out-of-plane emission of light enables its efficient collection, offering advantages for quantum applications where loss is a critical limitation [20]. Lastly, thanks to the minimal required processing of the $\chi^{(2)}$ nonlinear material, this approach is easily applicable to other materials that are challenging to process, yet host superb nonlinear optical properties [21, 22].

We begin the description of this idea in section 2, by establishing a theoretical framework for the VCOPO physics. We focus on a degenerate OPO configuration, where a pump beam at the second harmonic (SH) frequency generates a signal and idler at the fundamental harmonic (FH). Within this model, the figures of merit of a VCOPO are connected to the mode structure of the micro-cavity resonator at the FH and SH frequencies, which can be straightforwardly computed using numerical methods for a given device geometry. In section 3, we perform a case study of this architecture based on thin-film lithium niobate (TFLN). Using numerical simulations of the device performance, we layout the main considerations needed for realizing such a TFLN VCOPO pixel. We describe the design rules aiming at minimizing the oscillation threshold, by making both the SH and the FH resonant in the cavity (a.k.a. the doubly-resonant OPO), while maintaining quasi phase-matched interactions. Finally, in section 4 we explore selected applications based on the elements described above: dense meta-surfaces of parametric amplifiers, squeezers, and light emitters, as well as lattice simulators of two-dimensional many-body problems.

## 2. Model of a vertical cavity OPO

In this section, we derive a quantum model for a VCOPO and show how it relates to experimental figures of merits. For this, we employ theoretical frameworks established in existing literature [22–24].

### 2.1. Cavity mode structure

In figure 1, we illustrate the structure of a VCOPO device. One cell of a VCOPO is composed of two mirrors, one flat and the other curved. For simplicity, we assume the entire volume within the mirrors is filled with the $\chi^{(2)}$ nonlinear material.

The electric and magnetic fields inside a VCOPO can be parameterized through a modal expansion as

$$\mathbf{E}(x,y,z,t) = \sum_{\mu,m} \mathrm{e}^{-\mathrm{i}\omega_{\mu,m}t} a_{\mu,m} \mathbf{E}_{\mu,m}(x,y,z) \tag{1}$$

$$\mathbf{H}(x,y,z,t) = \sum_{\mu,m} \mathrm{e}^{-\mathrm{i}\omega_{\mu,m}t} a_{\mu,m} \mathbf{H}_{\mu,m}(x,y,z). \tag{2}$$

where the magnetic and electric field distributions $\mathbf{H}_{\mu,m}(x,y,z)$ and $\mathbf{E}_{\mu,m}(x,y,z)$ are the solutions to Maxwell's equations in the cavity, and $\mu$ and $m$ address the transverse and longitudinal mode orders, respectively. $a_{\mu,m}$ are complex mode-expansion coefficients, whose scale is determined by the energy, $U_{\mu,m}$, used to normalize $E_{\mu,m}$. For $U_{\mu,m} = \hbar\omega_{\mu,m}$, the dimensionless field amplitudes are normalized so that $|a_{\mu,m}|^2 = 1$ corresponds to one photon in the corresponding mode. In the limit where diffraction at the edges of the cavity can be ignored, the mode profile can be factorized as $\mathbf{H}_{\mu,m}(x,y,z) \approx \mathbf{H}_{\mu,m}(x,y)\cos(k_m z)$, with similar approximations for $\mathbf{E}_{\mu,m}$. In this limit, the longitudinal wavenumber $k_m$ is given by $k_m = 2\pi m/L$ with $m \in \mathbb{Z}$ and $L$ the length of the cavity.

### 2.2. Derivations of the Hamiltonian

In the presence of nonlinear interactions, the $\chi^{(2)}$ nonlinearity induces coupling between the FH and SH modes. To concisely address these modes, we label the SH amplitudes as $b_{\xi,\ell}$ while keeping $a_{\mu,m}$ for the mode amplitude of the FH field. The evolution of the fields follow the coupled-wave equations:

$$\partial_t a_{\mu,m} = \mathrm{i} \sum_{\nu,\xi} \sum_{n,\ell} g_{(\mu,\nu,\xi),(m,n,\ell)} a^*_{\nu,n} b_{\xi,\ell} \mathrm{e}^{\mathrm{i}(\omega_{\mu,m}+\omega_{\nu,n}-\omega_{\xi,\ell})t} \tag{3}$$

$$\partial_t b_{\xi,\ell} = \frac{\mathrm{i}}{2} \sum_{\mu,\nu} \sum_{m,n} g^*_{(\mu,\nu,\xi),(m,n,\ell)} a_{\mu,m} a_{\nu,n} \mathrm{e}^{-\mathrm{i}(\omega_{\mu,m}+\omega_{\nu,n}-\omega_{\xi,\ell})t}, \tag{4}$$

where the nonlinear coupling constant takes a form

$$g_{(\mu,\nu,\xi),(m,n,\ell)} = \frac{\epsilon_0 \hbar^{1/2} \omega_{\mathrm{SH}}^{1/2} \omega_{\mathrm{FH}}}{4 U_{\mu,m}^{1/2} U_{\nu,n}^{1/2} U_{\xi,\ell}^{1/2}} \times \sum_{i,j,k} \int \mathrm{d}V \chi^{(2)}_{i,j,k} E_{\mu,m,j} E_{\nu,n,k} E_{\xi,\ell,k}. \tag{5}$$

With the energy unit normalizing each mode as

$$U_{\mu,m} = \frac{1}{4} \int E^*_{\mu,m,i} \cdot \left(2\epsilon_{\mu,m,i,j} + \omega \partial_\omega \epsilon_{\mu,m,i,j}\right) \cdot E_{\mu,m,j} \mathrm{d}V. \tag{6}$$

And $\epsilon_{\mu,m,i,j}$ being the dielectric tensor elements at the frequency of mode $(\mu,m)$. Since the field profiles have cosine form in the longitudinal dimension $\propto \cos(k_m z)$, we can factor out the selection rule for longitudinal momentum as

$$g_{(\mu,\nu,\xi),(m,n,\ell)} = g_{\mu,\nu,\xi} \delta_{m+n,\ell}. \tag{7}$$

We now quantize the electro-magnetic field by promoting the complex field amplitudes to operators, and imposing the usual commutation relations $[\hat{a}_{\mu,m}, \hat{a}^\dagger_{\nu,n}] = \delta_{\mu,\nu}\delta_{m,n}$. The resulting field operators $\hat{a}_{\nu,n}$ and $\hat{b}_{\xi,\ell}$ annihilate photons in the respective modes of the FH and SH fields, respectively.

From these equations of motion, we can infer the form of the Hamiltonian in a rotating frame as (see detailed procedure in [22]):

$$\hat{H}_{MM} = \sum_{\mu,\nu,\xi} \sum_{m,n} \frac{\hbar g_{\mu,\nu,\xi} \delta_{m+n,\ell}}{2} \left(\hat{a}^\dagger_{\mu,m} \hat{a}^\dagger_{\nu,n} \hat{b}_{\xi,\ell} + \mathrm{H.c.}\right) + \sum_{\mu,m} \hbar\omega_{\mu,m} \hat{a}^\dagger_{\mu,m} \hat{a}_{\mu,m} + \sum_{\xi,\ell} \hbar\omega_{\xi,\ell} \hat{b}^\dagger_{\xi,\ell} \hat{b}_{\xi,\ell}. \tag{8}$$

This quantum multi-mode Hamiltonian and its relationship to the experimental cavity parameters highlighted above are the main results of this section. A scenario of primary interest is the coupling between the fundamental transverse modes of the cavity, for which we assign $\hat{a} = \hat{a}_{0,m}$, $\hat{b} = \hat{b}_{0,2m}$, $g = g_{000}$, $\omega_{\mathrm{FH}} = \omega_{m,0}$, and $\omega_{\mathrm{SH}} = \omega_{2m,0}$. The Hamiltonian simplifies to the familiar form:

$$\hat{H}_0 = \frac{\hbar g}{2}\left(\hat{a}^{\dagger 2}\hat{b} + \hat{a}^2\hat{b}^\dagger\right) + \hbar\omega_{\mathrm{FH}}\hat{a}^\dagger\hat{a} + \hbar\omega_{\mathrm{SH}}\hat{b}^\dagger\hat{b}. \tag{9}$$

### 2.3. Quantum equations of motion

To base the variety of functionalities the VCOPO can take on in the quantum regime, we continue to derive here the modal equations of motion in the language of operators. To make the formalisms concise, we move to a rotating frame given by a unitary operator $\hat{U}_{\mathrm{rot}} = \exp(-\mathrm{i}\omega_{\mathrm{SH}}(\hat{a}^\dagger\hat{a}/2 + \hat{b}^\dagger\hat{b}))$ in which the Hamiltonian $\hat{H}_0$ becomes

$$\hat{H}_{0,\mathrm{rot}} = \frac{\hbar g}{2}\left(\hat{a}^{\dagger 2}\hat{b} + \hat{a}^2\hat{b}^\dagger\right) + \hbar\Delta\hat{a}^\dagger\hat{a}, \tag{10}$$

where $\Delta = \omega_{\mathrm{FH}} - \omega_{\mathrm{SH}}/2$ is the detuning between the two coupled modes.

The evolution of the field operators is obtained in the Heisenberg picture through $\mathrm{i}\partial_t\hat{a} = \frac{1}{\hbar}[\hat{a}, \hat{H}]$. Adding Markovian dissipation terms for the two fields yields the following Heisenberg–Langevin equations:

$$\begin{aligned}
\mathrm{i}\partial_t\hat{a} =& g\hat{a}^\dagger\hat{b} + \Delta\hat{a} - \mathrm{i}\kappa_{\mathrm{FH}}\hat{a} - \mathrm{i}\sqrt{2\kappa_{\mathrm{FH,oc}}}\,\hat{a}_{\mathrm{oc}}(t) \\
&- \mathrm{i}\sqrt{2\kappa_{\mathrm{FH,int}}}\,\hat{a}_{\mathrm{int}}(t) \\
\mathrm{i}\partial_t\hat{b} =& \frac{g}{2}\hat{a}^2 - \mathrm{i}\kappa_{\mathrm{SH}}\hat{b} - \mathrm{i}\sqrt{2\kappa_{\mathrm{SH,oc}}}\,\hat{b}_{\mathrm{oc}}(t) \\
&- \mathrm{i}\sqrt{2\kappa_{\mathrm{SH,int}}}\,\hat{b}_{\mathrm{int}}(t),
\end{aligned} \tag{11}$$

where $\kappa_{\mathrm{c,oc}}$ and $\kappa_{\mathrm{c,int}}$ are out-coupling and intrinsic dissipation rates, respectively, with $c \in \{\mathrm{FH}, \mathrm{SH}\}$, which sum up to the total dissipation rates $\kappa_{\mathrm{c}} = \kappa_{\mathrm{c,oc}} + \kappa_{\mathrm{c,int}}$. The operators with 'oc' and 'int' subscripts are quantum fields associated to the out-coupling and intrinsic cavity loss, respectively.

### 2.4. Figures of merit

The above equations of motion allow to discuss the performance of the VCOPO in various applications, ranging from the classical to the quantum regime. The main figure of merit that determines the regime of operation of VCOPOs is the ratio between the non-linear coupling and the losses: $g/\kappa$, where $\kappa$ is the characteristic loss rate of the fields—to be specified in each context. This figure of merit determines the energy scale of any OPO: the higher it is, the fewer photons are needed to saturate the nonlinear optical behaviors. To see this more concretely, we now consider the VCOPO physics near threshold, relating this figure of merit to two experimentally relevant quantities: the OPO threshold power and the intra-cavity FH photon number.

We consider a classical model of a VCOPO by taking a mean-field approximation of the Heisenberg–Langevin equations (11), and ignore any higher-order correlations of the optical fields. As we consider the operation of the device as an OPO, we set the external seed field to zero, i.e. $\langle\hat{a}_{\mathrm{in}}(t)\rangle = 0$. Similarly, we have $\langle\hat{a}_{\mathrm{int}}(t)\rangle = \langle\hat{b}_{\mathrm{int}}(t)\rangle = 0$, as these fields are associated to the intrinsic dissipation and are not associated to excitable fields. The resulting equations of motions are:

$$\begin{aligned}
\mathrm{i}\partial_t\alpha &= g\alpha^*\beta + \Delta\alpha - \mathrm{i}\kappa_{\mathrm{FH}}\alpha \\
\mathrm{i}\partial_t\beta &= \frac{g}{2}\alpha^2 - \mathrm{i}\kappa_{\mathrm{SH}}\beta + \epsilon_{\mathrm{SH}},
\end{aligned} \tag{12}$$

where $\alpha = \langle\hat{a}\rangle$ and $\beta = \langle\hat{b}\rangle$ are the mean-field amplitudes of the signal and the pump modes, respectively. For an incoming pump power $P_{\mathrm{SH}}$, the field amplitude takes the form $\langle\hat{b}_{\mathrm{in}}\rangle = \mathrm{i}\sqrt{P_{\mathrm{SH}}/\hbar\omega_{\mathrm{SH}}}$, with which we define $\epsilon_{\mathrm{SH}} = \sqrt{2\kappa_{\mathrm{SH,oc}}}\langle\hat{b}_{\mathrm{in}}\rangle$. The steady-state of the system is obtained by finding solutions for $\partial_t\alpha = \partial_t\beta = 0$. Seeking for a condition at which a physical solution of non-zero $\alpha$ exists, we obtain

$$|\epsilon_{\mathrm{SH}}| \geqslant \frac{\kappa_{\mathrm{SH}}\sqrt{\kappa_{\mathrm{FH}}^2 + \Delta^2}}{g}, \tag{13}$$

where the OPO threshold corresponds to the point of equality. The resulting OPO threshold power reads

$$P_{\mathrm{SH,th}} = \frac{\hbar\omega_{\mathrm{SH}}\kappa_{\mathrm{SH}}^2\left(\kappa_{\mathrm{FH}}^2 + \Delta^2\right)}{2\kappa_{\mathrm{SH,oc}}g^2}, \tag{14}$$

which is directly related to the figure of merit $g/\kappa$.

Assuming $\Delta = 0$ for simplicity, the scaling of the threshold power reduces to $P_{\mathrm{SH,th}} \sim \kappa_{\mathrm{SH}}\kappa_{\mathrm{FH}}^2/g^2$. Similarly, the intra-cavity pump photon number in the saturated regime (i.e. above threshold) scales as

$$n_{\mathrm{SH,sat}} \sim \left(\frac{\kappa_{\mathrm{FH}}}{g}\right)^2. \tag{15}$$

Furthermore, the saturation signal photon number, i.e. the intra-cavity signal photon number at a pump power of $4P_{\mathrm{SH,th}}$ scales as

$$n_{\mathrm{FH,sat}} \sim \left(\frac{\sqrt{\kappa_{\mathrm{FH}}\kappa_{\mathrm{SH}}}}{g}\right)^2. \tag{16}$$

Again, this is directly given by the figure of merit with $\kappa$ set by a geometric mean of $\kappa_{\mathrm{FH}}$ and $\kappa_{\mathrm{SH}}$. In both cases, we find that the OPO is populated with smaller photon number even in the saturated regime when $g/\kappa$ is large.

It is therefore clear why $g/\kappa$ plays an essential role in determining when and how classical to quantum transitions occur in an OPO. Because vacuum quantum fluctuations of electromagnetic field are on the order of a single photon, we can ignore their contributions when the characteristic photon numbers are much larger than unity. Conversely, strong quantum contributions emerge when the number of pump photon at threshold approaches unity. We provide further discussions on this point in section 4.

## 3. Device design considerations

The above model now allows us to discuss a specific realization of the VCOPO. We describe the design-considerations aiming at minimizing the OPO threshold as much as possible. Equations (5) and (14) guide the design such that:

1. Each of the SH and the FH frequencies should match a cavity resonance, the so-called double-resonance condition.
2. The two modes should have a large overlap with each other and with the nonlinear material, and be phase matched.
3. Losses should be minimized, including: out-coupling through the cavity mirrors, scattering from rough surfaces, clipping, and absorption.

The proposed design is based on a doubly-resonant micro-cavity with the non-linear material sandwiched between two high reflectivity distributed Bragg reflectors (DBRs). While this resonant micro-cavity architecture limits the operation bandwidth of the device, it enables extremely low-power operation and highly scalable manufacturing. Within this framework, we discuss the design of the cavity considering the double-resonance and phase-matching conditions, transverse mode definition, and fine-tuning knobs. We finish by discussing the route to creating an array of such VCOPOs. To estimate our design's performances, the discussion is accompanied by numerical simulations of a VCOPO based on $X$-cut $LiNbO_3$ operating with a FH around 1560 nm when pumped by a SH around 780 nm wavelength, both polarized along the extraordinary axis of $LiNbO_3$.

### 3.1. Longitudinal design—resonance and phase-matching conditions

We begin the design of the cavity along the longitudinal coordinate, coarsely taking care of the resonances and phase-matching conditions in the cavity. These conditions can be phrased in terms of the phases accumulated by the fields over a cavity roundtrip, $\varphi_{\mathrm{FH}}$ and $\varphi_{\mathrm{SH}}$ for the FH and SH, respectively. The resonance conditions state that [25]:

$$\begin{cases} \varphi_{\mathrm{FH}} = 2k_{\mathrm{FH}}d + 2\varphi_{\mathrm{m,FH}} = 2\pi m, & m \in \mathbb{Z} \\ \varphi_{\mathrm{SH}} = 2k_{\mathrm{SH}}d + 2\varphi_{\mathrm{m,SH}} = 2\pi n, & n \in \mathbb{Z}. \end{cases} \tag{17}$$

The phase-matching condition between the FH and SH fields can be implemented at every half round-trip [26], by having the phase difference $\Delta\varphi_{\mathrm{m}}$ acquired upon reflection from one mirror compensate for the phase-mismatch accumulated while propagating one-way through the cavity:

$$\Delta\varphi_{\mathrm{m}} = (\varphi_{\mathrm{m,SH}} - 2\varphi_{\mathrm{m,FH}}) = -k_{\mathrm{SH}}d + 2k_{\mathrm{FH}}d \tag{18}$$

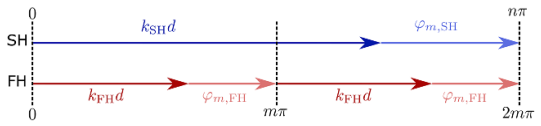


**Figure 2.** Cavity phase matching and double-resonance conditions. The vectors indicate the phases accumulated by the SH (top line) and FH (lower line) over half a round-trip in the cavity. We distinguish between the phases accumulated along the propagation in the cavity, $k_i d$, and the phases gained upon reflection by the mirror, $\varphi_{m,i}$. Phase-matching occurs when the mirror phase-mismatch compensates for the propagation phase-mismatch. Being resonant modes in the cavity, these phases amount to integer multiples of $\pi$, such that $n = 2m$.

These simple expressions show that phase-matching in the cavity can occur simultaneously with the double-resonance condition. Assuming the SH can be freely tuned to a resonance in the cavity, and phase-matching is achieved, then the FH is resonant if the SH mode order is even. Inversely, if both signals are resonant, and the SH longitudinal mode order is even, then phase-matching is obtained. In other words, for a SH wavelength near an even-ordered resonance of the cavity, the double resonance condition is met if and only if phase-matching is met as well. This results in the expected relationship between the SH and FH mode orders: $n = 2m$, such that all the chromatic dispersions of the cavity are balanced out, as depicted in figure 2.

To fulfill conditions (17) and (18) we follow the recipe proposed by Berger *et al* in [26], for enhancing second-harmonic generation (SHG) in a semiconducting vertical cavity:

1. One coherence length propagation: $(k_{SH} - 2k_{FH})L_{LN} = \pm\pi$, where $k_i$ ($i =$ FH, SH) is the wave-vector of the harmonics in the direction perpendicular to the cavity plane, and $L_{LN}$ is the $LiNbO_3$ slab thickness (for our example wavelengths this is about 10 $\mu$m).
2. Rephasing upon reflection: $\Delta\varphi_m = \varphi_{m,SH} - 2\varphi_{m,FH} = q\pi$, with $q$ an odd integer. In other words, the two harmonics are rephased after every pass through the cavity by the reflection phases of the DBR mirrors $\varphi_{m,i}$, ($i =$ FH, SH).

These cavity phase-matching conditions thus ensure that energy flows continually from the SH to the FH throughout the multiple cavity round-trips.

Through the proper design of the dielectric layers they are made of, DBRs offer the freedom to tailor both their reflection amplitude and phase profiles, to aid in the device performance. In particular, layer designs such as in references [26, 27] create two stop-bands, efficiently reflecting both the SH and the FH waves (lowering out-coupling losses) with the correct phases for phase-matching the cavity. Focusing on the micro-cavity design depicted in figure 3(a), we show in figure 3(b) the simulated reflection spectrum of such a dual stop-band DBR made of alternating layers of $SiO_2$ and $Ta_2O_5$ (with average refractive indices of 1.45 [28, 29] and 2.1 [28, 30], respectively), interfacing $LiNbO_3$ as the input medium, with refractive index based on Sellmeier and thermo-optic dependence [31]. This use of the bulk properties of $LiNbO_3$ is justified by its relatively large thickness, necessary for the above phase-matching recipe. The large refractive index difference between $SiO_2$ and $Ta_2O_5$ reduces the light penetration depth into these mirrors, contributing to stronger field confinement and interaction with the non-linear medium in the cavity. These materials also feature a very low absorption at the desired operating wavelength.

The double-resonance can be approximately obtained by controlling the non-linear slab thickness. We simulate this using a transfer-matrix formalism, that captures the fields at various wavelengths, their reflection, and their transmission along a cavity composed of planar layers. Figure 3(c) shows the simulated transmission spectra depending on the $LiNbO_3$ thickness, for the SH (left panel) and the FH (right panel) spectral domains. Multiple longitudinal mode orders, expressed as high transmission peaks, are visible for both the SH and FH. As the cavity length is swept, the minimal difference between the modes in the FH domain and the SH domain changes and approaches zero (see figure 3(d), blue curve). The steps-like behavior of the mode detuning is a consequence of choosing different pairs of closest FH and SH modes. As stated above, the minimal detuning is correlated with minimum half-roundtrip phase-mismatch, calculated assuming the SH is pumped resonantly, as shown in figure 3(d), red curve.

### 3.2. Transverse mode definition

On top of the longitudinal tuning of the cavity, it is essential to tune the transverse confinement of cavity modes. Its main benefit is in focusing the interacting fields, thus enhancing their local intensities and non-linear interaction (see equation (5)). The most intuitive route for the transverse mode confinement is to create plano-concave cavities through etching a dome in a capping layer or directly in the $LiNbO_3$, before depositing the top DBR mirror. Various gray-scale patterning approaches are applicable here, including

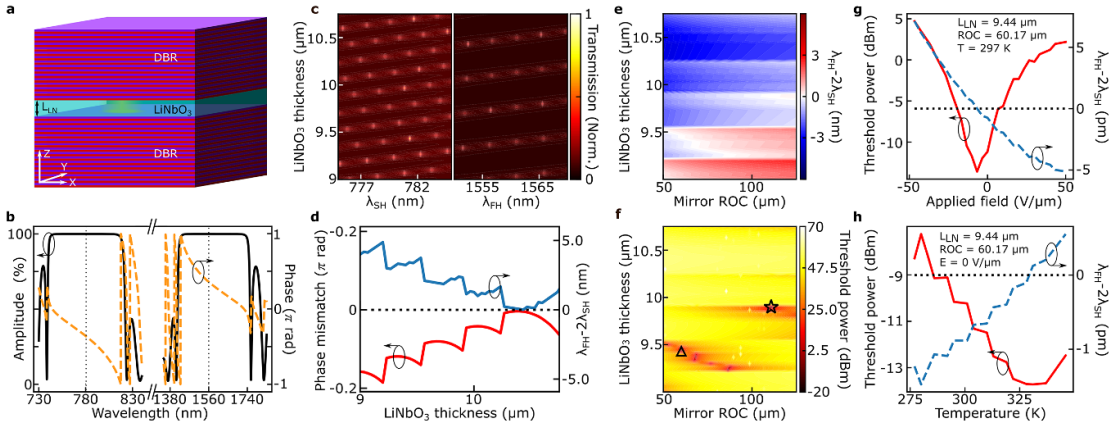


**Figure 3.** (a) Schematic of the VCOPO device. A slab of $LiNbO_3$ is embedded between two dual-stop-band DBRs. (b) Simulated reflection spectrum (amplitude—black, phase—dashed orange) of a single DBR with two stop-bands around 780 nm and 1560 nm. The DBR phase response provides approximately $\pi$ phase-mismatch between the two harmonics. (c) Simulated cavity transmission spectra around 780 nm (left) and around 1560 nm (right) as function of $LiNbO_3$ thickness. (d) Simulated phase mismatch between the SH and FH fields along half a cavity roundtrip, and detuning from double resonance condition as function of the $LiNbO_3$ thickness. (e), (f) Detuning from the double resonance condition (e) and estimated OPO threshold (f) as a function of the $LiNbO_3$ thickness and mirror ROC at 297 K, for the fundamental transverse Gaussian mode. The pump is kept in resonance with the SH cavity mode. (g), (h) Detuning (dashed line) and OPO threshold (continuous line) as function of DC electric field applied across the $LiNbO_3$ layer (g) and temperature (h). Cavity thickness: 9.44 $\mu$m, mirror ROC: 60.17 $\mu$m.

focused ion beam lithography [32], thermal scanning probe lithography [33], direct-write gray-scale lithography [34], polymer reflow techniques [35] or $CO_2$ laser ablation [36]. Moreover, several techniques to actively control the transverse confinement of photons have been reported in similar structures. For instance, Fe-doped $LiNbO_3$ was shown to allow photo-induced changes to its refractive index due to the photo-refractive effect [37]. This mechanism can be used to re-write the transverse profile of refractive index in the cavity through structured illumination by a control beam outside of the DBR stop-bands, thus tuning the mode confinement *in-situ* by the desired amount. Other approaches include controlled heat-induced mirror structuring [38], gain-lensing [39], and self-trapped spatial soliton formation [40].

Choosing the effective radius of curvature (ROC) of the transverse confining potential depends on several considerations. First, to maximize the nonlinear interaction in the cavity it is desired to focus the fields as much as possible, requiring as small as possible ROC. However, the stability of the cavity modes dictates a lower bound: the radius should be larger than the effective cavity length, including penetration depth into the DBRs. Generally it is preferred to work with even larger ROC, so that the mode diffraction is not significant, as well as to minimize clipping losses. The Gouy phase added to the oscillating modes by their transverse structure changes the resonance condition. To capture this effect, we simulate the transverse mode structure and Gouy phase using a Gaussian-beam matrix formalism (commonly named ABCD matrix). In this model, the DBRs are treated as ideal mirrors that are positioned so as to effectively account for the penetration depth of the resonant fields into the real DBR mirrors [41]. We then construct a cavity with two such mirrors, one with a flat surface and the other with a finite ROC and compute the profiles of the resonant modes. This two-step approach allows us to capture both the effect of Gaussian mode curvature and field interference on an equal footing and at low computational cost. Figure 3(e) displays the resulting detuning from double resonance $\Delta$, as function of the ROC and of the cavity thickness, for the fundamental transverse mode. Compared with figure 3(d), it shows that confining the modes shifts the minimal detuning to a shorter cavity length. It also demonstrates the existence of several 'bands' in which the detuning is close to zero, where different pairs of longitudinal modes are matched.

### 3.3. VCOPO threshold and performance analysis

Simulating the full geometry of the device, our calculation can estimate all the ingredients needed for the VCOPO threshold using equation (14). The detuning $\Delta$ is already obtained. The out-coupling loss rate, $\kappa_{oc}$, is estimated based on the power reflection coefficients of the DBRs, $R$, and the round-trip time in the cavity $\tau$, the inverse of the simulated free-spectral-range. Other loss factors (that comprise $\kappa_{int}$) are the absorption along the cavity roundtrip (absorption coefficient $\alpha$ from [42]), and the scattering due to surface-roughness [43, 44] (root-mean-square—rms—value, $\sigma$ based on state-of-the-art focused-ion-beam reports [45]). Those are expressed as follows, and added together for the total loss rate $\kappa$ (we omit the subscript identifying

**Table 1.** Design parameters and resulting OPO performance metrics of the simulated $LiNbO_3$ VCOPO. The lower part of the table corresponds to the anticipated metrics assuming the best reported surface roughness for $SiO_2$ micro-lenses. The important figures of merits, $g/\kappa$ and OPO threshold power, are shown in bold text.

| Parameter | Value at[a] | Value at △ |
|---|---|---|
| $L_{LN}$ ($\mu$m) | 9.9 | 9.43 |
| $R_{curve}$ ($\mu$m) | 110.8 | 60.13 |
| Surface rms roughness (nm) | 0.5 | 0.5 |
| $\lambda_{SH}$ (nm) | 787.191 | 779.548 |
| $\lambda_{FH}$ (nm) | 1574.383 | 1559.095 |
| Detuning (pm) | 0.79 | -1.25 |
| FH mode waist diameter ($\mu$m) | 3.22 | 2.68 |
| $g/2\pi$ (MHz) | 1.43 | 1.71 |
| $\kappa_{SH,oc}/2\pi$ (MHz) | 23.30 | 15.57 |
| $\kappa_{FH,oc}/2\pi$ (MHz) | 14.29 | 15.04 |
| $\kappa_{SH,i}/2\pi$ (MHz) | 0.92 | 0.97 |
| $\kappa_{FH,i}/2\pi$ (MHz) | 0.19 | 0.20 |
| $\kappa_{SH,s}/2\pi$ (MHz) | 274.78 | 291.89 |
| $\kappa_{FH,s}/2\pi$ (MHz) | 67.65 | 71.68 |
| $g/\kappa_{FH}$(%) | **1.75** | **1.97** |
| $P_{SH,th}$ ($\mu W$) | **46.15** | **104.96** |
| Best available rms roughness[a] (nm) | 0.17 | 0.17 |
| Corresponding $\kappa_{SH,s}/2\pi$ (MHz) | 31.76 | 33.74 |
| Corresponding $\kappa_{FH,s}/2\pi$ (MHz) | 7.82 | 8.29 |
| Corresponding $g/\kappa_{FH}$(%) | **6.50** | **7.38** |
| $P_{SH,th}$ (nW) at zero detuning | **46.60** | **44.21** |

[a]See [46].

the harmonic for brevity):

$$\kappa_{oc} = -\frac{1}{\tau}\ln R \tag{19}$$

$$\kappa_i = \frac{1}{\tau}\alpha L_{LN} \tag{20}$$

$$\kappa_s = \frac{1}{\tau}\left(\frac{4\pi\sigma}{\lambda}\right)^2 \tag{21}$$

$$\kappa = \kappa_{oc} + \kappa_i + \kappa_s. \tag{22}$$

The nonlinear coupling term $g$ is evaluated by the overlap integral of the simulated fields in the cavity, each normalized by the square-root of the calculated energy stored in it, $\sqrt{U_{FH}}$ and $\sqrt{U_{SH}}$:

$$g = \frac{\hbar^{\frac{1}{2}}\omega_{FH}\sqrt{\omega_{SH}\varepsilon_0}}{4U_{FH}\sqrt{U_{SH}}}\int dV\chi^{(2)}\left(E^*_{FH}(x,y,z)\right)^2 E_{SH}(x,y,z). \tag{23}$$

This expression is identical to equation (5), yet it uses the whole simulated fields and their stored energies, rather than their normalized spatial profiles. The field profiles are generated by a Gaussian beam-shape propagation along the medium, as provided by the beam-matrix simulation, dressed with the longitudinal sinusoidal, standing-wave-like, profile obtained by the transfer-matrix simulation. This also reveals the mode waist diameter (1/e), which defines the lower bound to the size of the device, below which clipping losses will become dominant.

A map of the calculated OPO threshold as function of $LiNbO_3$ thickness and mirror ROC is presented in figure 3(f). It clearly shows that the minimal pump power is required when the double-resonance condition is met. As discussed above, this condition is met at several different domains. For example, we list in table 1 the performance parameters for two close-to-optimal points at each of the observed bands, marked by a triangle and a star in figure 3(f).

The obtained threshold powers are limited by two factors. The most important parameter is the detuning from double-resonance: comparing the two analyzed points shows that while the triangle benefits from a larger $g/\kappa$, its OPO threshold power is higher, due to its larger deviation from double resonance. The second key parameter is the scattering losses due to mirror surface roughness. Indeed, the eighth-power dependence of the threshold on the rms mirror surface roughness implies that even slight improvements can significantly decrease the OPO threshold. In this context, the layered geometry of the VCOPO presents an advantage over

conventional waveguide geometries, as it avoids any sharp edges being etched onto the $LiNbO_3$. Thus, fine polishing and surface smoothing techniques can be utilized to enhance the device performance. For example, $CO_2$-laser ablation was shown to smoothen $SiO_2$ micro-lens surfaces down to 0.17 nm rms roughness [46]. Combined with $LiNbO_3$ micro-cavities, this would lower the scattering loss rates to 11.5% of our simulated values, thus enhancing $g/\kappa_{FH}$ to unprecedented values above 6%, with an on-resonance OPO threshold power reaching the tens of nW range (See the bottom lines in table 1). In this ideal regime, only $n_{SH,th} = 180$ pump photons in the cavity would suffice for the OPO to go above threshold, indicating the potential to realize novel quantum physics and functions, which we discuss in detail in section 4.

### 3.4. Fine-tuning

Our calculations so far show that because of the high finesse of the cavity, small deviations from the optimal ROC and cavity thickness result in orders-of-magnitude increase in the OPO threshold. Thus, achieving the double-resonance condition is key to the operation of VCOPO devices. For a post-fabricated VCOPO, this highlights the need for dynamic tuning knobs, that while not being strictly necessary for the device operation, can fine-tune the resonances of the VCOPO, help optimize its performance, and open the door to concerted operation of many devices.

As mentioned above, there are several available mechanisms for this purpose, generally modifying the refractive index and/or its distribution within the cavity. Two traditional approaches that we analyze here rely on tuning the refractive index of the nonlinear material by changing its temperature [31, 47] using micro-heaters, or by applying a DC electric field in the plane of the cavity (via the application of properly designed electrodes) and harnessing the Pockels (electro-optic) effect.

To demonstrate the performance of such knobs, we repeated the simulations of cavity tuning and OPO threshold for a specific choice of cavity thickness and ROC that are close to the optimal values. The effect of temperature was introduced through the temperature dependence of the refractive index of $LiNbO_3$[31]. The electric field effect used the relation: $\Delta n = -\frac{1}{2} n_0^3 r_{33} E_z$[48], where $n_0$ is the refractive index at zero applied field, and $r_{33} = 31\,\mathrm{pmV}^{-1}$[49] is the electro-optic coefficient for a field $E_Z$ along the extraordinary crystal axis, and light polarized along the same axis. The results are shown in figure 3(g), for electric field tuning, and figure 3(h) for the impact of temperature. With these fine-tuning simulations, we predict a minimal OPO threshold of 42.5 $\mu$W (–13.7 dBm). These simulations also show the potential of optimizing the device performance in a dynamic manner, offering, for example, to compensate small deviations from the optimal design.

### 3.5. Scalability

The small footprint of the proposed design enables the fabrication of dense two-dimensional VCOPO arrays that can operate in a concerted fashion towards classical and quantum photonic applications. The main challenge to surpass towards this goal is the non-uniformity of the non-linear material across the fabricated wafer. For example, thickness variations of about 5 nm over length-scales of a few millimeters are typical in state-of-the-art materials [50]. While this challenges the quality of OPO devices based on ring-waveguide geometries, the small footprint of the individual VCOPO makes it more robust to such large scale variations. Addressing the inhomogeneity across an entire array of VCOPOs can be done using the DBR ROC, or the fine-tuning knobs described above, provided that it is first mapped across a given wafer. The first parameter that compensates for variations in the cavity thickness is the ROC of the mirrors. Based on the map of the OPO threshold as function of the cavity thickness and ROC (figure 3(f)), the impact of small variations in cavity thickness can be counter-balanced by more significant changes to the ROC. This is an advantage, as this mitigation procedure requires much more relaxed control over the ROC than over the nonlinear material thickness. Furthermore, small inaccuracies in the designed ROC will not impact the performance a lot.

Altogether, we estimate that with reasonable control over the design parameters, low threshold VCOPOs can be realized, potentially reaching a regime where quantum-optical effects are manifested. Combined into arrays of VCOPO, this brings about a number of opportunities in generating or processing high-dimensional classical and quantum information, as we further discuss below.

## 4. Classical and quantum functions and applications of a VCOPO

In this section, we discuss possible functions and applications that may be uniquely enabled by a VCOPO's geometry and scalability, covering its operation from the classical, through the semi-classical, to the fully quantum regimes. To navigate this transition, an insightful perspective for when and how the classical-to-quantum transition occurs can be seen by partitioning the full quantum field to the classical mean-field and the quantum fluctuations parts:

$$\hat{a} = \alpha + \delta\hat{a} \qquad \hat{b} = \beta + \delta\hat{b}. \tag{24}$$

Here $\alpha$ and $\beta$ are complex numbers representing the classical mean field for the signal and pump modes, respectively; $\delta\hat{a}$ and $\delta\hat{b}$ are quantum fluctuations around the respective mean fields [15, 22, 51, 52]. Qualitatively different regimes of OPO physics occur depending on whether the quantum fluctuations play a considerable role compared to the classical mean-field part: (A) in the classical regime both $\delta\hat{a}$ and $\delta\hat{b}$ are negligible compared with the mean-field; (B) in the semi-classical regime $\delta\hat{b}$ is still negligible, but $\delta\hat{a}$ cannot be ignored (the signal field is quantum and the pump is classical); (C) in the fully quantum regime neither $\delta\hat{a}$ nor $\delta\hat{b}$ can be ignored, and all interacting fields are treated quantum-mechanically. Whether we can ignore quantum fluctuations depends essentially on the energy scale of the system, which is closely tied to the figure of merit $g/\kappa$, as discussed in section 2.4. We highlight below potential future applications of the VCOPO in each of these regimes, as well as the necessary conditions to achieve them.

### 4.1. Classical regime

When pumped above the critical power $P_{\mathrm{SH,th}}$, the OPOs goes above threshold, generating a large displacement to the signal field. As shown in section 2.4, the intra-cavity photon number around the threshold for pump and signal scales as (15) and (16), respectively. Therefore, when the ratio between the nonlinear coupling $g$ and the loss rate $\kappa$ is sufficiently small, i.e. $g/\kappa \ll 1$, both the signal and the pump fields have macroscopic amplitudes. This marks the classical regime of OPO, where the contributions from all of the quantum fluctuations are negligible.

The signal field couples out of the cavity as coherent radiation, which makes OPOs valuable light sources akin to lasers, with a large wavelength tunability range enabled by phase matching and resonance conditions. Generally, the functions and possible applications of a photonic device crucially depend on its geometry. The proposed surface-emitting geometry of a VCOPO would allow it to accommodate the function space currently occupied by VCSELs [53], with similar advantages of scalable mass production on a chip, small footprint, and parallelism, while offering the unique feature of frequency conversion.

This scalability is beneficial for applications that rely on multi-modal dynamics. One of such applications is a CIM [54]. A CIM leverages the collective oscillation behavior of an array of OPOs, where each OPO represents an Ising spin having two stable lasing states, i.e. 0 and $\pi$ phase offset relative to the pump light. The lasing pattern of a network of such coupled OPO can represent the solution to an Ising problem. A major challenge for realization of a large-scale CIM is the implementation of non-local couplings among OPOs. A leading architecture in the field uses a measurement-feedback approach [10, 11], where digital processors are used to mediate non-local effective interactions. However, such an approach based on electronics imposes limitations on speed and energy consumption of the system. A 2D array of VCOPOs coupled to free space offers a unique opportunity to tackle such a challenge. Advances in beam-shaping using spatial light modulators have made it plausible to control thousands to potentially millions of spatial modes [55]. By implementing inter-modal interactions directly via free-space optics, as has been conceived for VCSEL arrays [56], we envision a highly scalable all-optical CIM with VCOPOs.

The geometry of a VCOPO array also enables unique capabilities for amplifying spatially multiplexed signals in a phase sensitive manner. Such signals can be provided by free-space sources in the context of image intensifiers [57], or by multi-core fibers [58] for coherent telecommunications. Moreover, as recently demonstrated in [8, 59, 60], a high-gain optical parametric amplifier can play the role of a coherent homodyne detector. A 2D array of VCOPOs can thus be seen as an amplifier array with a capability to sense the phases of the incoming optical signals. Beyond the degenerate regime analyzed here, VCOPO arrays could find applications as frequency conversion layers for short-wavelength-IR and mid-IR imager technologies [61].

### 4.2. Semi-classical regime

When the VCOPO is pumped below threshold, the classical equations of motion (12) leads to zero mean field $\alpha = 0$. This, however, does not mean that no interesting dynamics occur because the quantum fluctuations $\delta\hat{a}$ can still have non-trivial dynamics, allowing it to operate as a parametric (i.e. phase-sensitive) amplifier. To see this, we consider the linearized evolution of the quantum fluctuations

$$\mathrm{i}\partial_t\hat{a} = r\hat{a}^\dagger + \Delta\hat{a} - \mathrm{i}\kappa_{\mathrm{FH}}\hat{a} - \mathrm{i}\sqrt{2\kappa_{\mathrm{FH,oc}}}\hat{a}_{\mathrm{in}}(t), \tag{25}$$

where $r = g\beta$ is the parametric gain driven by the classical pump field. Note that $\alpha = 0$ so $\hat{a} = \delta\hat{a}$ should be seen as quantum fluctuations. This equation shows how the signal fields inside an OPO experiences parametric gain, while the intra-cavity field is coupled to the external input field $\hat{a}_{\mathrm{in}}(t)$ and the output field $\hat{a}_{\mathrm{out}}(t)$ via the input-output relationship [62, 63]

$$\hat{a}_{\mathrm{out}}(t) = \hat{a}_{\mathrm{in}}(t) + \sqrt{2\kappa_{\mathrm{FH,oc}}}\hat{a}. \tag{26}$$

The output field of the OPO, $\hat{a}_{\rm out}(t)$, is given by the interference between the incoming signal field $\hat{a}_{\rm in}(t)$ and the transmitted intra-cavity field. Intuitively, the input optical signal $\hat{a}_{\rm in}(t)$ couples into the cavity to become $\hat{a}$, experiences parametric amplification/deamplification, and couples out as the outout signal $\hat{a}_{\rm out}(t)$. When no signal is sent to the input port, an OPO induces phase-sensitive amplification of the vacuum fluctuations, causing vacuum squeezing [20, 64–66]. This has been a primary means to produce non-classical light for quantum metrology, sensing, and computation.

Below, we estimate the squeezing level we could potentially achieve on a VCOPO. The level of attainable quadrature squeezing is maximized when an OPO is pumped just below the threshold. The variance of the squeezed quadrature relative to the vacuum fluctuation at this operation point takes the form

$$S = 1 - \overbrace{\frac{\kappa_{\rm FH,oc}}{\kappa_{\rm FH,oc} + \kappa_{\rm FH,int}}}^{\text{escape efficiency}}, \tag{27}$$

which is strongly connected to the escape efficiency, i.e. how much signal light couples out of the cavity before being lost. For example, in the case discussed in figure 3(h), the resulting squeezing is of $-0.82$ dB only, since the escape efficiency is only 17.3 %. However, one can in principle achieve an arbitrary degree of squeezing by making the cavity more over-coupled ($\kappa_{\rm FH,oc} \to \infty$), at the cost of increased pump power threshold $P_{\rm SH,th} \propto \kappa_{\rm FH}^2/g^2$. In practice, the maximum pump power that the system can handle will limit the level of achievable squeezing. While the reported damage threshold of Mg-doped $LiNbO_3$ strongly depends on the doping concentration, material composition, wavelength, temperature, etc we conservatively bound the discussion to average intra-cavity intensities no higher than 3 MW cm$^{-2}$. [67, 68] Returning to the design parameters discussed in relation to figure 3(h), keeping the intra-cavity pump intensity below that limit allows increasing $\kappa_{\rm FH}/2\pi$ to 761.5 MHz by increasing the out-coupling. Given $\kappa_{\rm FH,int}/2\pi = 85.88$ MHz, this indicates that a squeezing level of $-9.94$ dB can be attainable. Assuming a reduced surface roughness of 0.17 nm rms, we expect an even stronger squeezing level of $-19.4$ dB. Since the output modes of VCOPOs are naturally matched to free-space and optical fiber Gaussian modes, we anticipate that high degrees of squeezing can be maintained off-chip and efficiently distributed over networks.

### 4.3. Quantum regime

So far, we have ignored the contribution from the quantum fluctuations of the pump field. This is because a typical OPO is driven by a macroscopic classical field, i.e. $\beta \gg 1$, which is much greater than the nominal magnitude of quantum fluctuations. However, as the nonlinearity $g$ becomes comparable to the loss rate $\kappa$, we enter a regime where even tens to hundreds of pump photons suffice to bring an OPO above threshold. In such a deep quantum regime of an OPO, many more exotic quantum features arise due to the interaction between the quantum fluctuations of both signal and pump modes [15].

For instance, a phase-matched OPO above threshold with a large $g/\kappa$ can generate a coherent superposition of its classical bi-stable phase-configurations, forming a state similar to a Schrödinger's cat state inside the cavity [69]. When the OPO is phase-mismatched, on the other hand, the pump quadrature and signal modes effectively experience ponderomotive (i.e. opto-mechanical) interactions [70]. Consequently, information about the signal photon number gets coherently imprinted on the pump field. Thus, once detected outside the cavity, this entanglement collapses the intra-cavity state to a squeezed Fock state [71].

The threshold value of $g/\kappa$ above which we can observe such exotic quantum physics in nonlinear optics is an active field of research. While the strong coupling $g/\kappa > 1$ is typically seen as the classical-to-quantum cross-over point for few photon dynamics, there are several examples where having a mesoscopic number of pump photons can accelerate the nonlinear interactions and alleviate the requirement to $g/\kappa \sim 0.1$ [71, 72]. The full scope of non-Gaussian quantum physics of OPOs and experimental requirements to observe their signatures still remain to be unraveled.

A characteristic feature of this regime is the realization of non-Gaussian quantum states of light characterized by the negativities in their Wigner functions, which are associated with quantum contexuality and complexity [73]. An array of VCOPOs operated in the quantum regime can be a novel platform on which to study many-body non-Gaussian quantum physics of parametrically interacting bosons. More specifically, the Hamiltonian for a coupled array of VCOPO sites takes the form

$$\begin{aligned}\hat{H}/\hbar = &\sum_i \left\{ \frac{g}{2}\left(\hat{a}_i^{\dagger 2}\hat{b}_i + \hat{a}_i^2\hat{b}_i^\dagger\right) + \omega_{{\rm FH},i}\hat{a}_i^\dagger\hat{a}_i + \omega_{{\rm SH},i}\hat{b}_i^\dagger\hat{b}_i \right\} \\ &+ \sum_{ij}\left(J_{{\rm FH},ij}\hat{a}_i^\dagger\hat{a}_j + J_{{\rm SH},ij}\hat{b}_i^\dagger\hat{b}_j + {\rm H.c.}\right),\end{aligned} \tag{28}$$

which bears similarities to the canonical Bose–Hubbard model [74], but the interactions are now parametric. The coupling matrices $J_{ij}$ can be established by means of free-space coupling [56] or via the evanescent couplings between neighboring cavities. It is worth mentioning that the volume of literature on the many-body physics of such interactions is scarce [75]. This is in part because there has not been an easily accessible experimental platform that hosts such interactions (e.g. an atom does not normally split into two atoms). The proposed VCOPO platform could provide motivation to studying the physics of bosons interacting with parametric interactions.

For completeness, we note that when the nonlinearity $g/\kappa$ gets even larger to the extent of realizing the strong coupling condition $g/\kappa > 1$, we enter the regime where even the presence of a single photon can shift the energy of a cavity mode by more than the linewidth $\kappa$. Consequently, photon blockade is expected to happen [76], and the state space of each cavity becomes truncated, leaving two bottom states, i.e. vacuum state and a single-photon signal state. This creates a qubit-like subspace [77]. While this limit is not within reach based on the material nonlinearities and fabrication imperfections assumed in this work, the ability of a VCOPO to phase-match and cavity-enhance nonlinear interactions in virtually any $\chi^{(2)}$ material makes it a promising platform for future exploration of this frontier.

## 5. Conclusions

In this paper we proposed a blue-print for a new vertical cavity OPO design, capable of reaching extremely low oscillation threshold power and micrometer-scale footprint. Our proposed design is highly scalable, and only relies on already demonstrated metrics in terms of surface roughness, dielectric coatings, and material nonlinearities. Within a paraxial approximation, we derived the equations of motions for the FH and SH fields from first principles, and established explicit relationships between the experimentally relevant device parameters and the figures of merit of generic OPO devices. While the proposed design features $LiNbO_3$ as an exemplary intra-cavity non-linear material, we stress that this architecture is material-agnostic since both the modal confinement and quasi phase-matching conditions can be handled by the cavity mirrors design. In particular, our approach does not require high quality etching of the nonlinear material, nor periodic poling, and thus opens the door to realizing efficient non-linear interactions in a vast range of $\chi^{(2)}$ materials such as $NbOCl_2$ [78], 3R-$MoS_2$ [79], or InGaP [80]. Finally, we highlighted several potential applications of VCOPO devices, from tunable surface emitting OPO arrays to quantum-limited multi-mode amplifiers and new Hamiltonian simulators.

## Data availability statement

All data that support the findings of this study are included within the article (and any supplementary files).

## ORCID iDs

Ryotatsu Yanagimoto 0000-0002-9609-0076
Ouri Karni 0000-0003-0118-7033
Edwin Ng 0000-0002-3695-1698
Marc Jankowski 0000-0003-1845-7415
Timothy P McKenna 0000-0001-8132-7336
Thibault Chervy 0000-0003-2961-6805

## References

[1] Harris S E 1969 Tunable optical parametric oscillators *Proc. IEEE* **57** 2096
[2] Eckardt R C, Nabors C, Kozlovsky W J and Byer R L 1991 Optical parametric oscillator frequency tuning and control *J. Opt. Soc. Am. B* **8** 646
[3] Lu X, Moille G, Rao A, Westly D A and Srinivasan K 2020 On-chip optical parametric oscillation into the visible: generating red, orange, yellow and green from a near-infrared pump *Optica* **7** 1417
[4] Siegman A E 1962 Nonlinear optical effects: an optical power limiter *Appl. Opt.* **1** 127
[5] Pomarico E, Sanguinetti B, Gisin N, Thew R, Zbinden H, Schreiber G, Thomas A and Sohler W 2009 Waveguide-based opo source of entangled photon pairs *New J. Phys.* **11** 113042
[6] Tian Y, Wang Y, Wang W, Sun X, Li Y, Shi S, Tian L and Zheng Y 2025 Reservoir-engineered squeezed lasing through the parametric coupling *Phys. Rev. Lett.* **134** 243803
[7] Gu A, Sloan J, Roques-Carmes C, Choi S, Rosenthal E I, Horodynski M, Salamin Y, Vučković J and Soljačić M 2025 Quantum sensitivity of parametric oscillators *Phys. Rev. Res.* **7** L022056
[8] Roques-Carmes C, Salamin Y, Sloan J, Choi S, Velez G, Koskas E, Rivera N, Kooi S E, Joannopoulos J D and Soljačić M 2023 Biasing the quantum vacuum to control macroscopic probability distributions *Science* **381** 205
[9] The LIGO Scientific Collaboration 2011 A gravitational wave observatory operating beyond the quantum shot-noise limit *Nat. Phys.* **7** 962

[10] Honjo T *et al* 2021 100,000-spin coherent Ising machine *Sci. Adv.* **7** eabh0952
[11] McMahon P L *et al* 2016 A fully programmable 100-spin coherent Ising machine with all-to-all connections *Science* **354** 614
[12] Li G and Marandi A 2025 Turing-completeness and undecidability in coupled nonlinear optical resonators (arXiv:2501.06966)
[13] Lu J, Al Sayem A, Gong Z, Surya J B, Zou C-L and Tang H X 2021 Ultralow-threshold thin-film lithium niobate optical parametric oscillator *Optica* **8** 539
[14] Zhao M and Fang K 2022 InGaP quantum nanophotonic integrated circuits with 1.5% nonlinearity-to-loss ratio *Optica* **9** 258
[15] Yanagimoto R *et al* 2024 Mesoscopic ultrafast nonlinear optics-the emergence of multimode quantum non-gaussian physics *Optica* **11** 896
[16] Parto M, Li G H, Sekine R, Gray R M, Ledezma L L, Williams J, Roy A and Marandi A 2025 Ultrafast neuromorphic computing with nanophotonic optical parametric oscillators (arXiv:2501.16604)
[17] Canalias C and Pasiskevicius V 2007 Mirrorless optical parametric oscillator *Nat. Photon.* **1** 459
[18] Giordmaine J 1962 Mixing of light beams in crystals *Phys. Rev. Lett.* **8** 19
[19] Hum D S and Fejer M M 2007 Quasi-phasematching *C. R. Phys.* **8** 180
[20] Park T *et al* 2024 Single-mode squeezed-light generation and tomography with an integrated optical parametric oscillator *Sci. Adv.* **10** eadl1814
[21] Dutt A, Mohanty A, Gaeta A L and Lipson M 2024 Nonlinear and quantum photonics using integrated optical materials *Nat. Rev. Mater.* **9** 321
[22] Jankowski M, Yanagimoto R, Ng E, Hamerly R, McKenna T P, Mabuchi H and Fejer M 2024 Ultrafast second-order nonlinear photonics-from classical physics to non-gaussian quantum dynamics: a tutorial *Adv. Opt. Photonics* **16** 347
[23] Helt L and Sipe J 2022 Beyond photon pairs-nonlinear quantum photonics in the high-gain regime: a tutorial *Adv. Opt. Photonics* **14** 291
[24] Chen C-L 2006 *Foundations for Guided-Wave Optics* (Wiley)
[25] Siegman A E 1986 *Lasers* (University Science Books)
[26] Berger V 1997 Second-harmonic generation in monolithic cavities *J. Opt. Soc. Am. B* **14** 1351
[27] Apfel J H 1982 Phase retardance of periodic multilayer mirrors *Appl. Opt.* **21** 733
[28] Polyanskiy M N 2024 Refractiveindex.info database of optical constants *Sci. Data* **11** 94
[29] Malitson I H 1965 Interspecimen comparison of the refractive index of fused silica *J. Opt. Soc. Am.* **55** 1205
[30] Gao L, Lemarchand F and Lequime M 2012 Exploitation of multiple incidences spectrometric measurements for thin film reverse engineering *Opt. Express* **20** 15734
[31] Umemura N, Matsuda D, Mizuno T and Kato K 2014 Sellmeier and thermo-optic dispersion formulas for the extraordinary ray of 5 mol. % MgO-doped congruent $LiNbO_3$ in the visible, infrared and terahertz regions *Appl. Opt.* **53** 5726
[32] Dufferwiel S *et al* 2014 Strong exciton-photon coupling in open semiconductor microcavities *Appl. Phys. Lett.* **104** 192107
[33] Lassaline N, Thureja D, Chervy T, Petter D, Murthy P A, Knoll A W and Norris D J 2021 Freeform electronic and photonic landscapes in hexagonal boron nitride *Nano Lett.* **21** 8175
[34] Grushina A 2019 Direct-write grayscale lithography *Adv. Opt. Technol.* **8** 163
[35] Kharel P, Chu Y, Power M, Renninger W H, Schoelkopf R J and Rakich P T 2018 Ultra-high-*Q* phononic resonators on-chip at cryogenic temperatures *APL Photonics* **3** 066101
[36] Hunger D, Deutsch C, Barbour R J, Warburton R J and Reichel J 2012 Laser micro-fabrication of concave, low-roughness features in silica *AIP Adv.* **2** 012119
[37] Hesselink L, Orlov S S, Liu A, Akella A, Lande D and Neurgaonkar R R 1998 Photorefractive materials for nonvolatile volume holographic data storage *Science* **282** 1089
[38] Kurtscheid C, Dung D, Redmann A, Busley E, Klaers J, Vewinger F, Schmitt J and Weitz M 2020 Realizing arbitrary trapping potentials for light via direct laser writing of mirror surface profiles *Europhys. Lett.* **130** 54001
[39] DeSalvo R, Hagan D J, Sheik-Bahae M, Stegeman G, Van Stryland E W and Vanherzeele H 1992 Self-focusing and self-defocusing by cascaded second-order effects in KTP *Opt. Lett.* **17** 28
[40] Trillo S and Haelterman M 1998 Excitation and bistability of self-trapped signal beams in optical parametric oscillators *Opt. Lett.* **23** 1514
[41] Koks C and van Exter M P 2021 Microcavity resonance condition, quality factor and mode volume are determined by different penetration depths *Opt. Express* **29** 6879
[42] Leidinger M, Fieberg S, Waasem N, Kühnemann F, Buse K and Breunig I 2015 Comparative study on three highly sensitive absorption measurement techniques characterizing lithium niobate over its entire transparent spectral range *Opt. Express* **23** 21690
[43] Davies H 1954 The reflection of electromagnetic waves from a rough surface *Proc. IEE-Part IV: Inst. Monogr.* **101** 209
[44] Bennett H E and Porteus J 1961 Relation between surface roughness and specular reflectance at normal incidence *J. Opt. Soc. Am.* **51** 123
[45] Qu M, Shen Y, Wu L, Fu X, Cheng X and Wang Y 2020 Homogenous and ultra-shallow lithium niobate etching by focused ion beam *Precis. Eng.* **62** 10
[46] Najer D, Renggli M, Riedel D, Starosielec S and Warburton R J 2017 Fabrication of mirror templates in silica with micron-sized radii of curvature *Appl. Phys. Lett.* **110** 011101
[47] Gayer O, Sacks Z, Galun E and Arie A 2008 Temperature and wavelength dependent refractive index equations for MgO-doped congruent and stoichiometric $LiNbO_3$ *Appl. Phys. B* **91** 343
[48] Pockels F 1894 *Ueber den Einfluss des Elektrostatischen Feldes auf das Optische Verhalten piëZoelektrischer Krystalle* (Dieterichsche Verlags-Buchhandlung)
[49] Jazbinšek M and Zgonik M 2002 Material tensor parameters of LiNbO3 relevant for electro- and elasto-optics *Appl. Phys. B* **74** 407
[50] Xin C J *et al* 2025 Wavelength-accurate and wafer-scale process for nonlinear frequency mixers in thin-film lithium niobate *Commun. Phys.* **8** 1
[51] Ng E, Yanagimoto R, Jankowski M, Fejer M and Mabuchi H 2023 Quantum noise dynamics in nonlinear pulse propagation (arXiv:2307.05464)
[52] Uddin S Z, Rivera N, Seyler D, Salamin Y, Sloan J, Roques-Carmes C, Xu S, Sander M and Soljacic M 2023 Quantum sensitivity analysis: a general framework for controlling quantum fluctuations (arXiv:2311.05535)
[53] Seurin J-F, Xu G, Khalfin V, Miglo A, Wynn J D, Pradhan P, Ghosh C L and D'Asaro L A 2009 Progress in high-power high-efficiency vcsel arrays *Vertical-Cavity Surface-Emitting Lasers XIII* vol 7229 (SPIE) pp 19–29
[54] Yamamoto Y, Leleu T, Ganguli S and Mabuchi H 2020 Coherent ising machines-quantum optics and neural network perspectives *Appl. Phys. Lett.* **117** 160501

[55] Yang Y, Forbes A and Cao L 2023 A review of liquid crystal spatial light modulators: devices and applications *Opto-Electron. Sci.* **2** 230026
[56] Zhang D, Yuan Z, Hoang T X, Fu W, Png C E, Lim S T and Danner A 2025 All-optical scalable and programmable vcsel-based ising annealer with parallel feedback *Opt. Express* **33** 22119
[57] Lantz E and Devaux F 2008 Parametric amplification of images: from time gating to noiseless amplification *IEEE J. Sel. Top. Quantum Electron.* **14** 635
[58] Jain S *et al* 2017 32-core erbium/ytterbium-doped multicore fiber amplifier for next generation space-division multiplexed transmission system *Opt. Express* **25** 32887
[59] Nehra R, Sekine R, Ledezma L, Guo Q, Gray R M, Roy A and Marandi A 2022 Few-cycle vacuum squeezing in nanophotonics *Science* **377** 1333
[60] Kalash M and Chekhova M V 2023 Wigner function tomography via optical parametric amplification *Optica* **10** 1142
[61] Liu J *et al* 2022 A near-infrared colloidal quantum dot imager with monolithically integrated readout circuitry *Nat. Electron.* **5** 443
[62] Gardiner C W and Collett M J 1985 Input and output in damped quantum systems: quantum stochastic differential equations and the master equation *Phys. Rev. A* **31** 3761
[63] Metelmann A, Lanes O, Chien T, McDonald A, Hatridge M and Clerk A 2022 Quantum-limited amplification without instability (arXiv:2208.00024)
[64] Wu L-A, Xiao M and Kimble H 1987 Squeezed states of light from an optical parametric oscillator *J. Opt. Soc. Am. B* **4** 1465
[65] Dutt A, Luke K, Manipatruni S, Gaeta A L, Nussenzveig P and Lipson M 2015 On-chip optical squeezing *Phys. Rev. Appl.* **3** 044005
[66] McCuller L *et al* 2020 Frequency-dependent squeezing for advanced LIGO *Phys. Rev. Lett.* **124** 171102
[67] Bach F, Mero M, Chou M-H and Petrov V 2017 Laser induced damage studies of $LiNbO_3$ using 1030-nm, ultrashort pulses at 10-1000 kHz *Opt. Mater. Express* **7** 240
[68] Deng J, Zhang W, Wen J, Zhang G and Wang H 1994 Pulsed-laser-induced dark traces in $LiNbO_3$:Zn and $LiNbO_3$:Mg *Opt. Lett.* **19** 933
[69] Onodera T, Ng E, Gustin C, Lörch N, Yamamura A, Hamerly R, McMahon P L, Marandi A and Mabuchi H 2022 Nonlinear quantum behavior of ultrashort-pulse optical parametric oscillators *Phys. Rev. A* **105** 033508
[70] Qin W, Miranowicz A and Nori F 2022 Beating the 3 dB limit for intracavity squeezing and its application to nondemolition qubit readout *Phys. Rev. Lett.* **129** 123602
[71] Yanagimoto R, Nehra R, Hamerly R, Ng E, Marandi A and Mabuchi H 2023 Quantum nondemolition measurements with optical parametric amplifiers for ultrafast universal quantum information processing *PRX Quantum* **4** 010333
[72] Yanagimoto R, Nehra R, Ng E, Marandi A and Mabuchi H 2023 Engineering cubic quantum nondemolition hamiltonian with mesoscopic optical parametric interactions (arXiv:2305.03260)
[73] Walschaers M 2021 Non-gaussian quantum states and where to find them *PRX quantum* **2** 030204
[74] Freericks J and Monien H 1994 Phase diagram of the bose-hubbard model *Europhys. Lett.* **26** 545
[75] Bloch I, Dalibard J and Zwerger W 2008 Many-body physics with ultracold gases *Rev. Mod. Phys.* **80** 885
[76] Birnbaum K M, Boca A, Miller R, Boozer A D, Northup T E and Kimble H J 2005 Photon blockade in an optical cavity with one trapped atom *Nature* **436** 87
[77] Mabuchi H 2012 Qubit limit of cavity nonlinear optics *Phys. Rev. A* **85** 015806
[78] Guo Q *et al* 2023 Ultrathin quantum light source with van der Waals $NbOCl_2$ crystal *Nature* **613** 53
[79] Trovatello C *et al* 2025 Quasi-phase-matched up-and down-conversion in periodically poled layered semiconductors *Nat. Photon.* **19** 291
[80] Akin J, Zhao Y, Misra Y, Haque A N and Fang K 2024 InGaP $\chi^{(2)}$ integrated photonics platform for broadband, ultra-efficient nonlinear conversion and entangled photon generation *Light Sci. Appl.* **13** 290